Enhancement of Electrical Conductivity of Transparent Ga-Doped Zinc Oxide Films via Quench Reduction in an Atmospheric Pressure Plasma Jet

Pin-Han Chou (周品涵), Jing-Chi Huang (黃京淇), Kuo-Long Pan (潘國隆),[†]
and Jia-Yang Juang (莊嘉揚)[*]
Department of Mechanical Engineering, National Taiwan University, Taipei 10617, Taiwan (R.O.C.)

(Received 29 April 2019; revised manuscript received 14 August 2019; published 25 September 2019)

An atmospheric pressure plasma jet (APPJ) is used to deposit highly transparent and conductive impurity doped zinc oxide thin films. Although studies have shown that plasma reactivity can be affected due to quenching by O_2 from the ambient air in the downstream, the correlation between the quenching effect and thin film properties has not yet been demonstrated. We propose a nozzle design with an additional feature for reducing the quench. We perform comprehensive numerical simulations, considering gas-phase reaction kinetics and turbulent flow, to show that the O_2 quenching is indeed significantly reduced. We prepare Ga-doped ZnO (GZO) films using the modified APPJ system and confirm that both resistivity and deposition rate are improved. Moreover, we obtain a low resistivity of $3.3 \times 10^{-4}\ \Omega\,\mathrm{cm}$ in open air, which is comparable to GZO films prepared by the state-of-the-art sputtering tools. The physical insight and concept may be applied to other subjects of plasma reactions in atmospheric ambience where surrounding oxygen may yield significant quenching and reduce overall performance, for instance, in medical and surface treatments.

DOI: 10.1103/PhysRevApplied.12.034050

I. INTRODUCTION

Transparent conductive oxides (TCOs) are widely used as electrodes in flat panel displays and solar cells [1], and are of increasing importance since they are often the key materials that limit the performance of emerging devices, such as tandem solar cells [2]. Indium tin oxide (ITO), with a resistivity as low as $1\text{–}2 \times 10^{-4}\ \Omega\,\mathrm{cm}$, is the best TCO available today for mass production. Driven by the increasing price of indium, research efforts have been made to search for viable alternatives. Among them, aluminum and gallium doped ZnO (AZO and GZO) have attracted much attention due to their comparable optoelectronic properties, low resistivity in the range of $2-4 \times 10^{-4}\ \Omega\,\mathrm{cm}$, nontoxicity, and abundance in the earth's crust [3–5].

We have routinely deposited GZO films using nitrogen atmospheric pressure plasma jet (APPJ) [6–10]. Compared to sputtering, the most common deposition method, APPJ does not require a vacuum chamber and is suitable for a continuous in-line process. However, since the deposition is done in open air, it is more susceptible to environmental air flow and temperature influences. For instance, oxygen entrainment into the jet downstream can significantly quench the excited nitrogen molecules and reduce their concentration, leading to a decrease in plasma reactivity [11–14]. Tsai *et al.* performed numerical simulations of a nitrogen APPJ using laminar and turbulent flow models coupled with gas-phase reaction kinetics [13]. They found that the turbulent model is required to correctly predict the quenching effect, gas temperature, and NO density. Despite the extensive numerical and experimental studies on the effect of quenching on the plasma characteristics of APPJ systems, whether the optoelectronic properties and deposition rate of ZnO films can be improved by reducing the quenching effect is still unknown.

The objectives of this study are threefold. First, we propose an alternative nozzle design with a "nozzle hat," a feature intended to reduce the quenching effect. Second, we develop a three-dimensional numerical model following the approach presented in Tsai *et al.* [13], but include an additional reaction to simulate the formation of ZnO [15,16]. Third, we prepare GZO films using the modified APPJ system and confirm that their resistivity and deposition rate are indeed improved due to the reduction in oxygen quenching. Also, ZnO is a highly defective material and defects play an important role in resistivity [3,17,18]. We carry out material characterizations and discuss the possible source of resistivity improvement.

II. NUMERICAL SIMULATIONS

We perform numerical simulations of the nitrogen atmospheric pressure plasma jet with and without a nozzle hat, considering the gas-phase reaction kinetics and turbulent flow (k-ϵ model). The case without the nozzle hat is the

*jiayang@ntu.edu.tw
†panpeter@ntu.edu.tw

 © 2019 American Physical Society

standard configuration and has been used in our previous works [6–10]. The nozzle hat, a 60-mm circular thin plate installed on the nozzle exit, is introduced in the present study to reduce the oxygen entrainment into the jet downstream (Fig. 1). We use the commercial package COMSOL Multiphysics and follow the method presented by Tsai *et al*. [13]. In addition, we include the reaction of the precursor to study the formation of ZnO, which is not included in Ref. [13]. We consider 12 kinds of species, including nitrogen molecule (N_2), nitrogen radical (N), nitrogen excited states $A^3\sum_u^+$ [N_2(A)], $B\ ^3\Pi_g$ [N_2(B)], $C\ ^3\Pi_u$ [N_2(C)], $a'\sum_u^-$ [N_2(a)], oxygen molecule (O_2), oxygen radical (O), ozone (O_3), nitrogen monoxide (NO), nitrogen dioxide (NO_2), and nitrous oxide (N_2O). The reactions in the model are shown in Table I. The electron density of the plasma region is assumed as a uniform constant, and the electron density (n_e) and electron temperature (T_e) are set to 10^{16} m^{-3} and 3 eV, respectively [19]. The plasma undergoes glow discharge in a very short time, but the process is limited by the simulation, so it is assumed that this process is a natural steady state. By setting the electron density and the electron temperature to fixed values, it is expected to provide the discharge consequence of the plasma source.

Zinc nitrate is treated as the precursor at the inlet and its reactions occur within the system as shown in Table II. The gas temperature is considered to be the thermal decomposition temperature in the calculation.

The chemical model used in the simulation is the transport of concentration species: $\omega_j = 1 - \sum_i \omega_i$, $D(-D_i\nabla C_i + C_i u_i) = R_i$, $\omega_i = C_i \times M_i$, and $M = \left(\sum_i \frac{\omega_i}{M_i}\right)^{-1}$, where ω_i and ω_j are, respectively, the mass fractions of species i and j. The sum of the mass fractions of all species is 1. R_i is the mass production rate of species i. M is the average mole mass; M_i, C_i, D_i, and u_i are, respectively, the mole mass, concentration, diffusion coefficient, and diffusion direction of the species i.

The boundary conditions of the simulation are shown in Fig. 1(a). At the main gas inlet, 20 slm (standard liter per minute) N_2 at 300 K is provided and at the precursor inlet, $Zn(NO_3)_2$ at 353 K is input. To represent the arc reactions, we assume a high temperature, 1200 K, at the electrode. For the case with the nozzle hat, a thin plate with a radius of 30 mm is added at the nozzle exit, that is, the outlet of the plasma jet. The distance between the nozzle exit and the substrate is 2 mm.

We validate the accuracy of the three-dimensional numerical approach on grid convergence. Via the analysis of the velocity distribution over the substrate, we demonstrate that as the number of grid cells increases, the variation in the velocity profile is reduced. Furthermore, considering the quenching effect near the center of the plasma head as computed by the three different grid meshes, the difference in the magnitude is within 1%.

Figure 2 shows the simulation results of the distributions of the streamlines, the concentration of ZnO, and the quenching reactions of the two cases. The nitrogen flow of the standard configuration [Fig. 2(a)] is more disordered than the case with the nozzle hat [Fig. 2(b)]. The nozzle hat constrains the gas flowing outside the nozzle and reduces the interference, mixing, and turbulence of the gas near the nozzle exit (the deposition zone), potentially leading to a smoother distribution of ZnO concentration and reduced oxygen from the atmosphere.

Figures 2(c) and 2(d) show the comparison of the distribution of ZnO concentration on the vertical cross section and on the substrate between the two cases. The

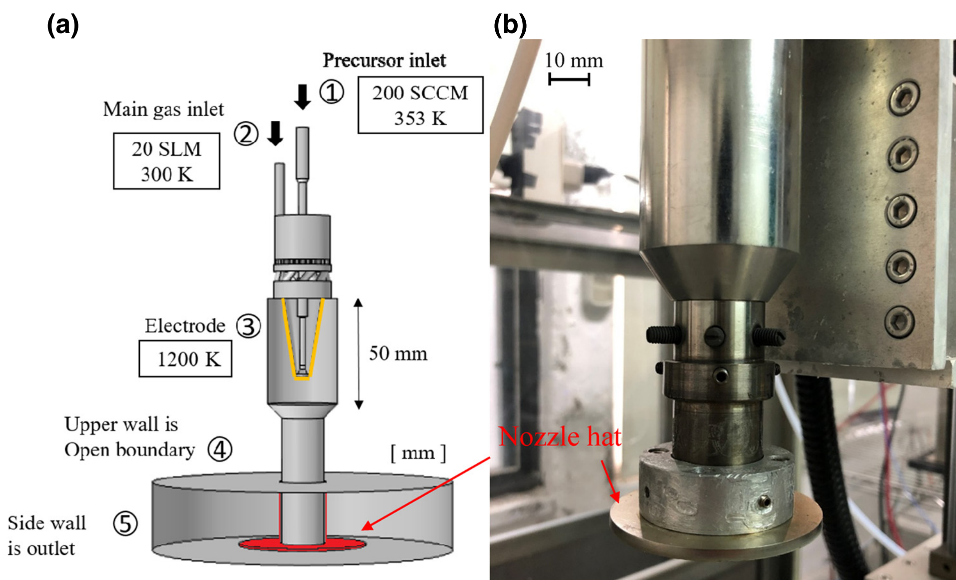

FIG. 1. (a) Schematic of the numerical model and boundary conditions used in the simulations. (b) Photograph of the nozzle and nozzle hat.

TABLE I. Reactions for the nitrogen plasma.

No.	Reaction	Reaction rate constant (cm^3 s^{-1})	Ref.
R_1	$N + N + M \rightarrow N_2 + M$	$8.3 \times 10^{-34} \exp(500/T)$[a]	[20]
R_2	$N_2 + N + N \rightarrow N_2(A) + N_2$	$8.27 \times 10^{-34} \exp(500/T)$[a]	[21]
R_3	$N_2(A) + N_2 \rightarrow N_2 + N_2$	4×10^{-17}	[22]
R_4	$N_2(A) + N \rightarrow N_2 + N$	9.6×10^{-11}	[21]
R_5	$N + N + M \rightarrow N_2(B) + M$	$8.3 \times 10^{-34} \exp(500/T)$[a]	[21]
R_6	$N_2(A) + N_2(A) \rightarrow N_2(B) + N_2$	7×10^{11}	[21]
R_7	$N_2(B) \rightarrow N_2(A) + h\nu$	1.5×10^{5}[b]	[21]
R_8	$N_2(B) + N_2 \rightarrow N_2(A) + N_2$	5×10^{-11}	[21]
R_9	$N_2(C) \rightarrow N_2(B) + h\nu$	3×10^{7}[b]	[21]
R_{10}	$N_2(C) + N_2 \rightarrow N_2(a) + N_2$	10^{-11}	[21]
R_{11}	$N_2(A) + N_2(A) \rightarrow N_2(C) + N_2$	3×10^{-10}	[21]
R_{12}	$N_2(a) + N_2 \rightarrow N_2(B) + N_2$	2×10^{-13}	[21]
R_{13}	$N_2(a) + O_2 \rightarrow N_2 + O + O$	2.8×10^{-11}	[21]
R_{14}	$N_2(a) + NO \rightarrow N_2 + N + O$	3.6×10^{-10}	[21]
R_{15}	$N + NO \rightarrow O + N_2$	$1.05 \times 10^{-12} \times T^{0.5}$	[21]
R_{16}	$N + O_2 \rightarrow O + NO$	$4.5 \times 10^{-12} \exp(-3220/T)$	[21]
R_{17}	$N + O + M \rightarrow NO + M$	$1 \times 10^{-32} \times (300/T)^{0.5}$[a]	[20]
R_{18}	$N_2(A) + O_2 \rightarrow N_2 + O + O$	2.54×10^{-12}	[21]
R_{19}	$N_2(A) + NO \rightarrow N_2 + NO$	7×10^{-11}	[21]
R_{20}	$N_2(B) + NO \rightarrow N_2(A) + NO$	2.4×10^{-10}	[21]
R_{21}	$N_2(B) + O_2 \rightarrow N_2 + O + O$	3×10^{-10}	[21]
R_{22}	$O + O + M \rightarrow O_2 + M$	$2.8 \times 10^{-34} \exp(720/T)$[a]	[20]
R_{23}	$N + NO_2 \rightarrow 2O + N_2$	9.1×10^{-13}	[21]
R_{24}	$e + N_2 \rightarrow N + N + e$	$1.249 \times 10^{-10} \times (11608T_e)^{0.49} \exp(-13.78/T_e)$	[23]
R_{25}	$N + NO_2 \rightarrow N_2 + O_2$	7×10^{-13}	[21]
R_{26}	$N + NO_2 \rightarrow 2NO$	2.3×10^{-12}	[21]
R_{27}	$e + N_2 \rightarrow N_2(A) + e$	$1.23 \times 10^{-6} \times (11608T_e)^{-0.47} \exp(-8.7/T_e)$	[23]
R_{28}	$O + NO \rightarrow NO_2 + h\nu$	4.2×10^{-18}	[20]
R_{29}	$O + NO_2 \rightarrow NO + O_2$	$1.13 \times 10^{-11} \exp(T/1000)^{0.18}$	[21]
R_{30}	$O + NO + M \rightarrow NO_2 + M$	$6.34 \times 10^{-32} \exp(300/T)^{1.8}$[a]	[21]
R_{31}	$e + N_2 \rightarrow N_2(B) + e$	$4.06 \times 10^{-5} \times (11608T_e)^{0.74} \exp(-10.07/T_e)$	[23]
R_{32}	$NO_2 + NO_2 \rightarrow 2NO + O_2$	$3.3 \times 10^{-12} \exp(-13500/T)$	[20]
R_{33}	$N + O_3 \rightarrow NO + O_2$	2×10^{-16}	[21]
R_{34}	$O + O_3 \rightarrow O_2 + O_2$	$2 \times 10^{-11} \exp(-2300/T)$	[21]
R_{35}	$NO + O_3 \rightarrow O_2 + NO_2$	$4.3 \times 10^{-12} \exp(-1560/T)$	[21]
R_{36}	$O + O_2 + M \rightarrow O_3 + M$	$5.8 \times 10^{-34} \exp(300/T)^{2.8}$[a]	[20]
R_{37}	$N + NO_2 \rightarrow N_2O + O$	3×10^{-12}	[21]
R_{38}	$N_2(A) + O_2 \rightarrow N_2O + O$	7.8×10^{-14}	[21]
R_{39}	$N_2(A) + N_2O \rightarrow N_2 + N + NO$	10^{-11}	[21]
R_{40}	$O + N_2O \rightarrow NO + NO$	$1.5 \times 10^{-10} \exp(-14900/T)$	[20]
R_{41}	$e + N_2 \rightarrow N_2(C) + e$	$1.85 \times 10^{-11} \times (11608T_e)^{1.5747} \exp(-2.3658/T_e)$	[23]
R_{42}	$e + N_2 \rightarrow N_2(a) + e$	$8.3 \times 10^{-11} \times (1.5T_e)^2 \exp(-3.43/T_e)$	[23]

[a]Rate constant unit is cm^6 s^{-1}.
[b]Rate constant unit is s^{-1}.

total concentration of the species is the volume integral of the overall model, an indication of the efficiency of the APPJ system. After installing the nozzle hat, the total ZnO concentration increases by approximately 120% from 4.0338×10^{-15} mol to 8.8668×10^{-15} mol. The uniformity on the substrate is also improved with the hat, which may help improve the uniformity of the deposited film.

It is known that the nitrogen excited state molecule [$N_2(B)$] in nitrogen plasma is highly susceptible to the concentration of oxygen in the air [13]. During the energy transfer process, the nitrogen excited state molecules [$N_2(B)$] can easily react with oxygen molecules in the atmosphere through the reaction of $R21$, resulting in loss of energy. This phenomenon is known as quenching and can be quantified by the reaction rate distributions of $R21$ as shown in Figs. 2(e) and 2(f). The average reaction rate density decreases from 2.3622×10^{14} m^{-6} to 8.9648×10^{13} m^{-6} (−60%) as the nozzle hat is included. For the standard configuration, the reaction rate is high on

TABLE II. Reaction of the formation of ZnO.

No.	Reaction	Reaction rate constant s^{-1}	Ref.
*R*1	$2Zn(NO_3)_2 \overset{373\,K}{\rightarrow} 2ZnO + 4NO_2 + O_2$	$8.154 \times 10^{12}(298/T)^{-10.92}$ $\exp(-17521/T)$	[16]

the substrate near the nozzle exit and in a region within the nozzle [Fig. 2(e)]. In contrast, after installing the nozzle hat, the region with high reaction rates is pushed out and located outside of the nozzle hat. This minimizes the quenching effect in the region where the formation of ZnO takes place (*R*1 in Table II) and may explain the increase of ZnO concentration discussed earlier.

III. EXPERIMENTAL VERIFICATION: THIN FILM DEPOSITION AND CHARACTERIZATION

To verify the simulation results, we deposit GZO thin films on glass substrates (50×50 mm^2) by APPJ with and without a nozzle hat. The experimental details are similar to our published works [6,7,9,10] and are summarized as

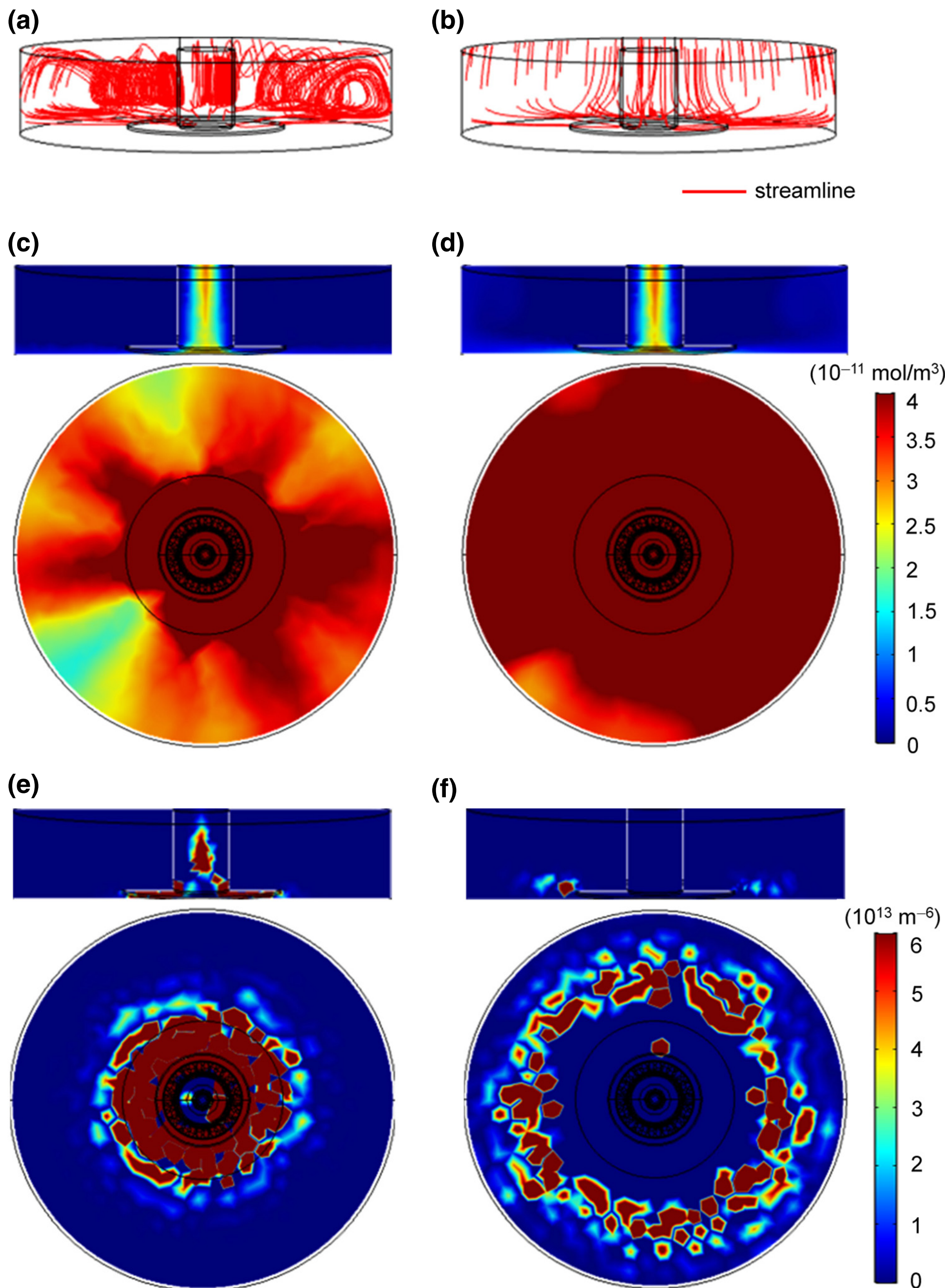

FIG. 2. Comparison of the simulation results between the standard configuration (left column) and the modified configuration with the nozzle hat (right column). (a),(b) The streamline distributions. (c),(d) The ZnO concentrations. (e),(f) The distributions of the reaction rate of *R*21. Average values are 2.3622×10^{14} m^{-6} and 8.9648×10^{13} m^{-6} for the standard and modified configurations, respectively.

follows. The APPJ system consists of a plasma jet, a direct current (dc) pulsed power source, an ultrasonic atomizer, a hot plate (200 °C), and computer-controlled *x*-*y*-*z* stage. The pulse frequency, duty cycle, and applied voltage are 27.78 kHz, 22.2%, and approximately 6.4 kV, respectively. The precursor is composed of zinc nitrate [$Zn(NO_3)_2$, J.T. Baker, 99.6% purity] and gallium nitrate [$Ga(NO_3)_3$, Alfa Aesar, 99.9% purity] and has an atomic percentage of $Ga/(Ga + Zn)$ equal to 8%. The mist of the precursor generated with ultrasonic atomizer at 2.45 MHz is injected into the plasma chamber by carrier gas, which is blended with 140 sccm (standard cubic centimeter per minute) nitrogen and 60 sccm forming gas (93% argon + 7% hydrogen). Nitrogen used as plasma working gas with a flow rate of 20 slm flows through a Teflon tube inside the plasma chamber. GZO films are deposited on glass substrates (50×50 mm^2). The experiments are conducted under two different nozzle designs—the standard and the modified. Different from the standard one, the modified nozzle has a thin circular plate with a radius of 30 mm and a thickness of 3 mm attached to its nozzle exit. Other conditions are the same for both cases. The distance between the nozzle and substrate is 2 mm and the scanning pitch in the *y* axis is 2 mm. The power of the hot plate, which maintains the substrate temperature at 200 °C, is 500 W. Electrical resistivity, Hall mobility, and carrier concentration are measured by the Hall Effect (Ecopia HMS-3000) in the van der Pauw configuration at room temperature. A UV-Visible-NIR spectrophotometer (Jasco V-670) is used to determine the optical transmittance of GZO film. The temperatures measured by thermocouples positioned on the glass substrate are recorded by a data logger (GRAPHTEC GL-840) with a sampling rate of 20 Hz. The concentration depth profiles of Ga and Si are measured by Secondary Ion Mass Spectrometer (time of flight secondary ion mass spectrometer, TOF SIMS).

Figure 3(a) shows the electrical resistivity, Hall mobility, and carrier concentration of GZO films deposited with and without the nozzle hat are characterized by the Hall effect measurement. For the case with the hat, the carrier concentration increases significantly from 1.58×10^{21} cm^{-3} to 2.03×10^{21} cm^{-3} (+28.5%) and the resistivity is reduced from 3.8×10^{-4} Ω cm to 3.3×10^{-4} Ω cm (−13%). Furthermore, Hall mobility decreases from 10.58 cm^2 V^{-1} s^{-1} to 9.45 cm^2 V^{-1} s^{-1} (−10.7%). The decrease of mobility may be attributed to the increase of carrier concentrations through a mechanism known as impurity scattering and impurity clustering [1,3].

Figure 3(b) shows the comparison of the optical transmittance over the UV-Visible-NIR regime. Samples 1–3 are prepared using the standard nozzle, whereas samples 4–6 are prepared with the nozzle hat. In the visible spectra, the transmittance of samples 4–6 is comparable to that of samples 1–3, and the average transmittances of all samples are higher than 80%, making them suitable for flat panel applications. However, in the near-infrared regime, the transmittance of samples 4–6 drops much more than that of samples 1–3 because of the free carrier absorption, a phenomenon more pronounced at high carrier concentrations [3,24]. Such a drop of the near-infrared transmittance between 800 and 1200 nm is not desirable when those films are used as a front contact in a top cell in tandem applications, as it blocks low-energy photons from passing through [2].

Figure 4 shows the SIMS measurement of the concentration depth profiles of Ga and Si in the GZO films deposited with and without the nozzle hat. Inspection of the results highlights two key observations. First, samples 4–6 exhibit higher Ga concentrations (approximately +20%) than samples 1–3 [Fig. 4(a)]. Since substitutional gallium (Ga_{Zn}) is the major donor of the free carriers in GZO films [3], a higher level in Ga concentration can explain the higher carrier concentration observed in the

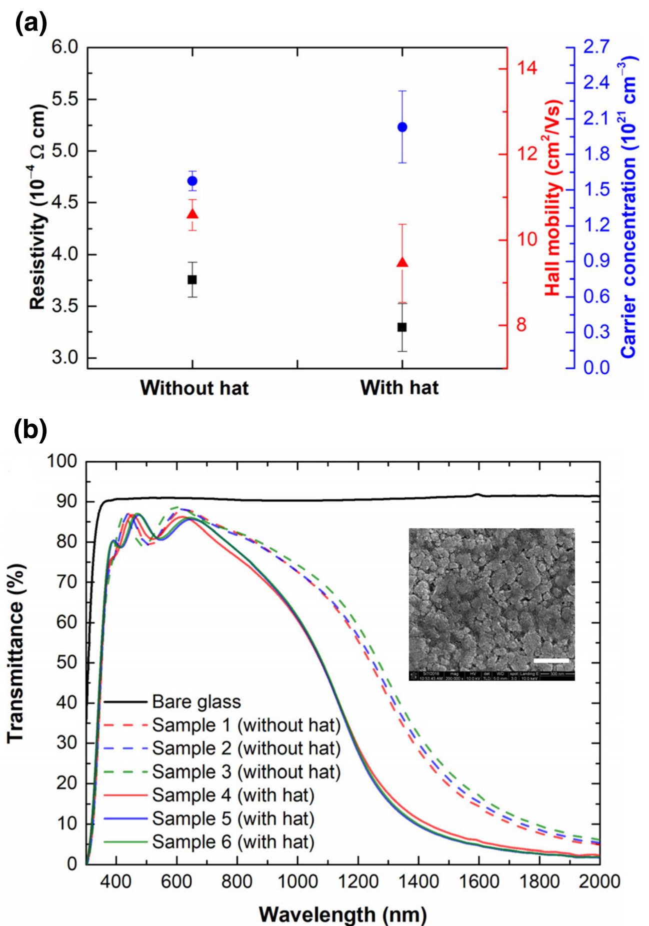

FIG. 3. Optoelectronic properties of the deposited GZO films. (a) Hall measurements and (b) transmittance spectra. Inset: A representative SEM image of the GZO films (scale bar: 300 nm). The morphology of the samples prepared with and without the plasma hat is not distinguishable, indicating that the film microstructure is not responsible for the improvement of film resistivity.

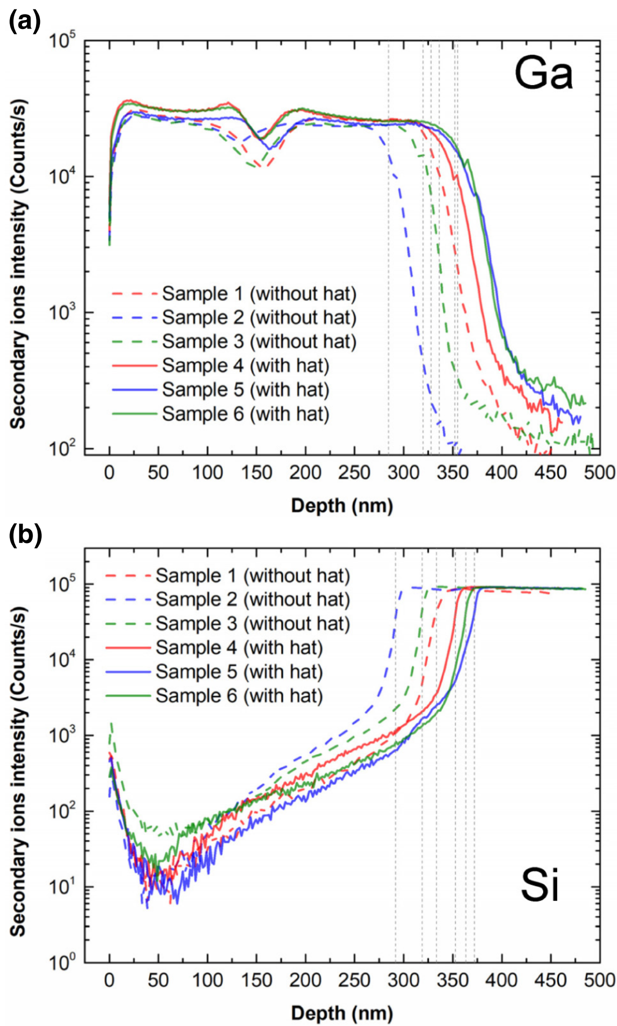

FIG. 4. SIMS measurement of the concentration depth profiles of Ga (a) and Si (b) in the GZO films deposited with and without the nozzle hat.

Hall measurement of samples 4–6 [Fig. 3(a)]. The increase of Ga doping in the GZO films may be attributed to the enhanced plasma reactivity as the nozzle hat reduces the quenching effect. Second, samples 4–6 are also thicker (approximately +18% from 310 ± 20 nm to 362 ± 8 nm) as estimated by the concentration depth profiles of Si [Fig. 4(b)]. Since the total deposition time is the same for all samples (approximately 14 min each), a thicker film implies a higher deposition rate. The average deposition rate over the entire sample size increases from approximately 22 nm/min to approximately 26 nm/min (sample size: 50×50 mm^2) after the nozzle hat is installed. Such an increase in deposition rate is consistent with the increase of ZnO concentration as shown in Figs. 2(c) and 2(d). The instantaneous deposition area, assuming the *x*-*y* scanning motion does not occur, is approximately equal to the nozzle size, which is a circle with a diameter of 20 mm, and the corresponding rate is approximately 207 nm/min. Note that the film profile is not uniform under such a condition.

Deposition temperature—the temperature on the substrate where the deposition takes place—has been well regarded as an important factor to influence the properties of impurity-doped ZnO films [25–28]. To investigate whether the observed improvement in the electrical conductivity and deposition rate is due to the deposition temperature, we use thermocouples and a data logger to measure the substrate temperature under the centerline of the nozzle. The temperature slightly decreases from 648 to 641 K as the nozzle hat is installed. We also obtain the substrate temperature at the same location from our numerical model. The values are, respectively, 632.7 and 613 K for the cases with and without the nozzle hat. The simulated temperatures are, in general, consistent with the experimental ones. The simulated temperature of the case with the nozzle hat is approximately 20 K higher than that of the standard one, which is the opposite to the experimental result. Such a discrepancy may be due to the fact that our numerical simulation cannot accurately count the heat transfer between the fluid and the solid wall.

IV. CONCLUSIONS

In summary, we develop a coupled-field finite element model, considering the gas-phase plasma reaction kinetics and turbulent flow, to predict the plasma reaction rates, the ZnO concentration, and the quenching effect of APPJ systems. Our simulation results show that adding a circular thin plate, that is, the nozzle hat, on the nozzle exit can effectively reduce the quenching of the excited nitrogen molecules due to oxygen entrainment from the ambient air, leading to higher plasma reactivity and higher and smoother ZnO concentration. Our experiments show that the GZO films deposited with the nozzle hat exhibit a lower resistivity (−12.25%) and a higher deposition rate (+18%), compared to those deposited with the standard configuration. We obtain a low resistivity of $3.3 \times 10^{-4}\ \Omega$ cm in open air, which is comparable to GZO films prepared by the state-of-the-art sputtering tools. Limitations of our present model include: (1) the precursor is zinc nitrate instead of the actual composition of zinc nitrate and gallium nitrate. (2) The resultant ZnO is gas phase instead of the actual solid phase. These are interesting and challenging topics for future work. The concept of the present work may be extended to various areas sharing similar ingredients, specifically plasma reactions and carrying flows, for example, medical and surface treatments [29–33]. In such conditions, a vacuum environment is often not applicable and so the plasma reactions would be subject to similar effects of quenching as studied herein. Therefore, local management and/or isolation of surrounding flows based on simple geometry could readily reduce

the adverse contribution of ambient oxygen and sustain plasma reactivity.

ACKNOWLEDGMENTS

This work is supported by National Taiwan University (Grants No. NTU-108L891006 and No. NTU-107L89 1006) and the Ministry of Science and Technology (MOST) of Taiwan (Grants No. 106-2221-E-002-123-MY3 and No. 104-2221-E-002-022-MY2). We thank Professor I-Chun Cheng and Professor Cheng-Che Hsu for helpful discussions. We thank Hsiao-Ping Hsu for technical support and Pei-Rong Li for assistance in the computational approach.

P.-H.C. and J.-C.H. contributed equally to this work.

[1] K. Ellmer, Past achievements and future challenges in the development of optically transparent electrodes, Nat. Photonics **6**, 809 (2012).

[2] F. Fu, T. Feurer, T. P. Weiss, S. Pisoni, E. Avancini, C. Andres, S. Buecheler, and A. N. Tiwari, High-efficiency inverted semi-transparent planar perovskite solar cells in substrate configuration, Nat. Energy **2**, 16190 (2016).

[3] K. Ellmer, A. Klein, and B. Rech, *Transparent Conductive Zinc Oxide : Basics and Applications in Thin Film Solar Cells* (Springer, Berlin, 2008), Springer series in materials science, 104.

[4] E. Fortunato, L. Raniero, L. Silva, A. Gonçalves, A. Pimentel, P. Barquinha, H. Águas, L. Pereira, G. Gonçalves, I. Ferreira, E. Elangovan, and R. Martins, Highly stable transparent and conducting gallium-doped zinc oxide thin films for photovoltaic applications, Sol. Energy Mater. Sol. Cells **92**, 1605 (2008).

[5] K. L. Chopra, S. Major, and D. K. Pandya, Transparent conductors-A status review, Thin Solid Films **102**, 1 (1983).

[6] J. Y. Juang, H. T. Lin, C. T. Liang, P. R. Li, W. K. Chen, Y. Y. Chen, and K. L. Pan, Effect of ambient air flow on resistivity uniformity of transparent Ga-doped ZnO film deposited by atmospheric pressure plasma jet, J. Alloys Compd. **766**, 868 (2018).

[7] Y. Y. Chen and J. Y. Juang, Enhancement of Ga-doped zinc oxide film properties and deposition rate by multiple deposition using atmosphere pressure plasma jet, J. Alloys Compd. **694**, 452 (2017).

[8] Y. Y. Chen and J. Y. Juang, Finite element analysis and equivalent parallel-resistance model for conductive multilayer thin films, Meas. Sci. Technol. **27**, 074006 (2016).

[9] T. S. Chou, H. T. Lin, Y. Y. Chen, K. L. Pan, and J. Y. Juang, Effect of main gas and carrier gas on ZnO thin films deposited by atmospheric pressure plasma jet, Thin Solid Films **594**, 282 (2015).

[10] J. Y. Juang, T. S. Chou, H. T. Lin, Y. F. Chou, and C. C. Weng, Trajectory effect on the properties of large area ZnO thin films deposited by atmospheric pressure plasma jet, Appl. Surf. Sci. **314**, 1074 (2014).

[11] C.-C. Hsu and C.-Y. Wu, Electrical characterization of the glow-to-arc transition of an atmospheric pressure pulsed arc jet, J. Phys. D: Appl. Phys. **42**, 215202 (2009).

[12] C. C. Hsu and Y. J. Yang, The increase of the jet size of an atmospheric-pressure plasma jet by ambient air control, IEEE Trans. Plasma Sci. **38**, 496 (2009).

[13] J. H. Tsai, C. M. Hsu, and C. C. Hsu, Numerical simulation of downstream kinetics of an atmospheric pressure nitrogen plasma jet using laminar, modified laminar, and turbulent models, Plasma Chem. Plasma Process. **33**, 1121 (2013).

[14] Y. W. Hsu, Y. J. Yang, C. Y. Wu, and C. C. Hsu, Downstream characterization of an atmospheric pressure pulsed arc jet, Plasma Chem. Plasma Process. **30**, 363 (2010).

[15] C. C. Addison, J. Lewis, and R. Thompson, 628. The liquid dinitrogen tetroxide solvent system. Part VII. Products of reaction of zinc with liquid dinitrogen tetroxide, J. Chem. Soc. **1**, 2829 (1951).

[16] I. D. Campbell, E.S.R. investigation of the thermal decomposition of zinc nitrate hexahydrate, J. Chem. Soc., Faraday Trans. **73**, 487 (1977).

[17] T. Ruf, S. Repp, J. Urban, R. Thomann, and E. Erdem, Competing effects between intrinsic and extrinsic defects in pure and Mn-doped ZnO nanocrystals, J. Nanopart. Res. **18**, 109 (2016).

[18] H. Kaftelen, K. Ocakoglu, R. Thomann, S. Tu, S. Weber, and E. Erdem, EPR and photoluminescence spectroscopy studies on the defect structure of ZnO nanocrystals, Phys. Rev. B **86**, 1 (2012).

[19] G. V. Naidis, Simulation of convection-stabilized low-current glow and arc discharges in atmospheric-pressure air, Plasma Sources Sci. Technol. **16**, 297 (2007).

[20] M. Capitelli, *Plasma Kinetics in Atmospheric Gases* (Springer, Berlin, New York, 2000), Springer series on atomic, optical, and plasma physics, 31.

[21] I. A. Kossyi, A. Yu Kostinsky, A. A. Matveyev, and P. V. Silakov, Kinetic scheme of the non-equilibrium discharge in nitrogen-oxygen mixtures, Plasma Sources Sci. Technol. **1**, 207 (1992).

[22] M. Moravej, X. Yang, M. Barankin, J. Penelon, S. E. Babayan, and R. F. Hicks, Properties of an atmospheric pressure radio-frequency argon and nitrogen plasma, Plasma Sources Sci. Technol. **15**, 204 (2006).

[23] Y. Itikawa, Cross sections for electron collisions with oxygen molecules, J. Phys. Chem. Ref. Data **38**, 1 (2006).

[24] H. Peelaers, E. Kioupakis, and C. G. Van De Walle, Fundamental limits on optical transparency of transparent conducting oxides: Free-carrier absorption in SnO_2, Appl. Phys. Lett. **100**, 1 (2012).

[25] S.-M. Park, T. Ikegami, and K. Ebihara, Effects of substrate temperature on the properties of Ga-doped ZnO by pulsed laser deposition, Thin Solid Films **513**, 90 (2006).

[26] T. Yamada, A. Miyake, S. Kishimoto, H. Makino, N. Yamamoto, and T. Yamamoto, Effects of substrate temperature on crystallinity and electrical properties of Ga-doped ZnO films prepared on glass substrate by ion-plating method using DC arc discharge, Surf. Coat. Technol. **202**, 973 (2007).

[27] S. Kim, J. Jeon, H. W. Kim, J. G. Lee, and C. Lee, Influence of substrate temperature and oxygen/argon flow ratio on the electrical and optical properties of Ga-doped ZnO thin films prepared by rf magnetron sputtering, Cryst. Res. Technol. **41**, 1194 (2006).

[28] A. Bikowski and K. Ellmer, Influence of the deposition temperature on electronic transport and structural properties

of radio frequency magnetron-sputtered $Zn_{1-x}Mg_xO : Al$ and $ZnO : Al$ films, J. Mater. Res. **27**, 2249 (2012).

[29] O. V. Penkov, M. Khadem, W.-S. Lim, and D.-E. Kim, A review of recent applications of atmospheric pressure plasma jets for materials processing, J. Coat. Technol. Res. **12**, 225 (2015).

[30] Y. F. Hong, J. G. Kang, H. Y. Lee, H. S. Uhm, E. Moon, and Y. H. Park, Sterilization effect of atmospheric plasma on Escherichia coli and Bacillus subtilis endospores, Lett. Appl. Microbiol. **48**, 33 (2009).

[31] H. W. Lee, S. H. Nam, A. A. H. Mohamed, G. C. Kim, and J. K. Lee, Atmospheric pressure plasma jet composed of three electrodes: Application to tooth bleaching, Plasma Process. Polym. **7**, 274 (2010).

[32] G. Daeschlein, T. Von Woedtke, E. Kindel, R. Brandenburg, K. D. Weltmann, and M. Jünger, Antibacterial activity of an atmospheric pressure plasma jet against relevant wound pathogens in vitro on a simulated wound environment, Plasma Process. Polym. **7**, 224 (2010).

[33] K. D. Weltmann, E. Kindel, R. Brandenburg, C. Meyer, R. Bussiahn, C. Wilke, and T. von Woedtke, Atmospheric pressure plasma jet for medical therapy: Plasma parameters and risk estimation, Contrib. Plasma Phys. **49**, 631 (2009).